Foteini Lamprou, Marine Sciences, dept. Geosciences

A biomarker-based paleotemperature record over the last 3 million years west off Tasmania

Foteini Lamprou (6979505)

1st Supervisor: Peter Bijl

2nd Supervisor: Suning Hou

Marine Sciences

Utrecht University

11/01/2023

Abstract

The last 3 Ma is a crucial period for the Earth's climate evolution as it went through the transition from a warm mid-late Pliocene (~3.2 Ma) into the colder late Pliocene- early Pleistocene (~2.5 Ma), with larger ice sheets and high amplitude glacial to interglacial cycles. During the Mid Pleistocene Transition (MPT), in the field of palaeoceanography, the Southern Ocean has been proposed as one of the key regions of the global ocean, as during the Quaternary, subantarctic waters of the Southern Ocean cooled by 4-9^{o}C, as a result of a northward movement of the fronts in the Indian Ocean sector, the Great Australian Bright and the Tasmanian regions. The sedimentary record around Tasmania thus represents a perfect archive to record the oceanographic conditions in this region and especially the latitudinal position of the Subtropical Front (STF), which emerged as a key parameter in the global climate due to its influence on Atlantic Meridional Overturning Circulation (AMOC) and the Indian and Atlantic Oceans. We here present the continuous BAYSPAR and BAYSPLINE-based SST record of the Subtropical Front in the Southern Ocean at Ocean Drilling Program (ODP) Site 1168 in western Tasmania, to identify the consequences of the SST changes observed at this site, for the oceanographic conditions, specifically the strength and the position of the subtropical front. This extra record of SST change is a long-term high-resolution analysis of organic geochemistry proxies and yields a better understanding of the influence of Antarctica and the Southern Ocean on Late Pliocene and Quaternary based on temperature proxies. Previous studies (Bostock et al., 2015; Sikes et al., 2009) in this area, focused on the isotope signals which are significantly influenced by other factors, such as seasonality or rainfall, presenting a short-term analysis, however, here we present a long-term continuous high-resolution analysis of temperature records based on organic geochemistry proxies for the late Pliocene and Quaternary.

Lower reflectance values, at Site 1168, were reported during interglacial periods while higher values were depicted during glacial, indicating that glacial sediments mainly consist of foraminifera ooze while interglacial sediments mainly contain nannofossil ooze. SST records decrease from 3 to approximately 1.3 Ma, on average 6 degrees to 4 degrees, and then increase until modern, presenting a constant variability in temperature of 9 to 18 degrees throughout the record. Subtropical Front (STF) faced an extremely low value of 3-4^{o}C during MIS16, at approximately 0.6 Ma and after this period STF SST eventually increases to the modern levels of about 16 to 23 ^{o}C. However, our results suggest that non-thermal factors, such as water column oxygenation and nutrient supply, may influence GDGT cyclization which is linked to some cold bias in the TEX_{86}-based SST records. Site 1168 presents a temperature difference of 9-18 degrees throughout the records, except the early Pleistocene period (~2.3 Ma); this variability is higher than the equatorial sites which is a sign of polar amplification and it is closely related to glacial-interglacial migration of the subtropical front, resulting in a northward movement of STF and a shift of the Subtropical Convergence to ~42^{o}S west of Tasmania, at approximately 0.02 Ma.

Contents

1. Introduction

The late Neogene and Quaternary faced the Mid-Pliocene warm period (mPWP, 3.264 -3.025 Ma) and the expansion of Northern Hemisphere ice sheets, as well as the progressive amplification of glacial-interglacial variability (Leutert et al., 2021) and characterized by large continental ice sheets in the Northern Hemisphere(Hodell & Warnke, 1991). The glaciation increase began at approximately 3.1 Ma and culminated at 2.5-2.4 Ma, near the Gauss/ Matuyama boundary (Hodell & Warnke, 1991); the boundary between the Pliocene and Pleistocene epochs (Fig 1.). Since this period, when the Quaternary started, the Earth's climate has been generally in a glacial mode, marked by over 50 repetitive cycles (Hodell & Warnke, 1991). Quaternary was characterized as a cold period and the general trend is cooler temperatures and larger ice sheets (Da et al., 2019; Hodell & Venz-Curtis, 2006). Most Plio-Pleistocene climate research has focused on two relatively abrupt climate transitions, the onset of major Northern Hemisphere glaciation (~2.7Ma) and the mid-Pleistocene transition (MPT) (~0.9 Ma) (Lisiecki & Raymo, 2007). The former occurred within the increase of ice volume between 3.6 and 2.4 Ma and also the progressive Cenozoic cooling, providing the necessary conditions for major Northern Hemisphere glaciation (Head et al., 2008), while the latter is a glacial to interglacial transition, the transition from 41kyr obliquity cycle to 100kyr eccentricity and it remains unknown exactly what forced this change (Ford et al., 2016; Ford & Chalk, 2020).

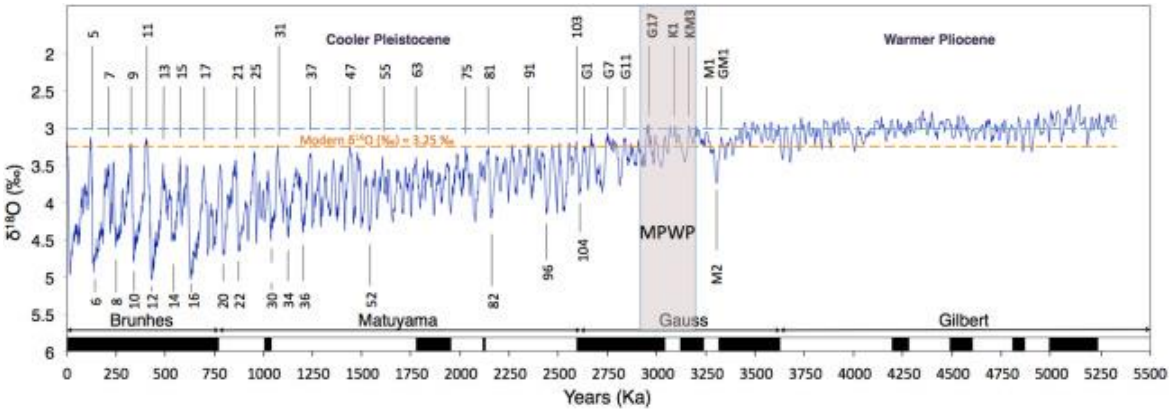

Figure 1. The LR04 Stack with magnetic chrons and subchrons indicated by black bars along the x-axis; MPWP = mid-Pliocene warm period; blue dashed line represents mean δ18O value between 3.32 and 5.32 Myr; orange dashed line is the mean δ18O value of last 5 kyr of Holocene; the data includes a + 0.64‰ Cibicidoides vital effect correction and selected marine isotope stages (MIS) are indicated, source: (Lisiecki and Raymo, 2005).

The relative contribution of Northern Hemisphere versus Southern Hemisphere ice sheets in this transition, and the interplay between Southern Hemisphere ice sheets and the oceanography of the Southern Ocean, is still unknown. However, the Southern Ocean (SO) is one of the key global ocean regions, through its role in global ocean circulation and atmospheric carbon uptake (Rintoul, 2018). The SO has a strong influence not only on the ocean and atmospheric circulation but also on the global scales climate (Rintoul, 2018), through its continuous gaseous exchanges with the atmosphere and because of its unique circulation pattern (Rintoul, 2018; Sallée, 2018). It connects the world's major ocean basins because of the flow of the Antarctic Circumpolar Current (ACC) and through the deep-water formation, as it links the atmosphere to the deep sea (below ~2,500 m) and provides the principal connections between the deeper and shallow layers of the global ocean circulation (Rintoul, 2018) (Fig. 2b). Moreover, the tilted isopycnals and eddies transport fluid and tracers across the ACC and in return deep water reach the sea surface near Antarctica (Hodell & Venz-Curtis, 2006; Rintoul, 2018). Interactions between the atmosphere, ocean, and cryosphere lead to the transformations of water masses, such as Antarctic Bottom Water (AABW), Subantarctic Mode Water (SAMW), and Antarctic Intermediate Water (AAIW), resulting in an overturning circulation; this overturning circulation sets the capacity of the ocean to store and transport carbon dioxide and heat. Therefore, any change in the Southern Ocean can have massive global ocean and climate consequences (Hodell & Venz-Curtis, 2006; Rintoul, 2018; Sallée, 2018).

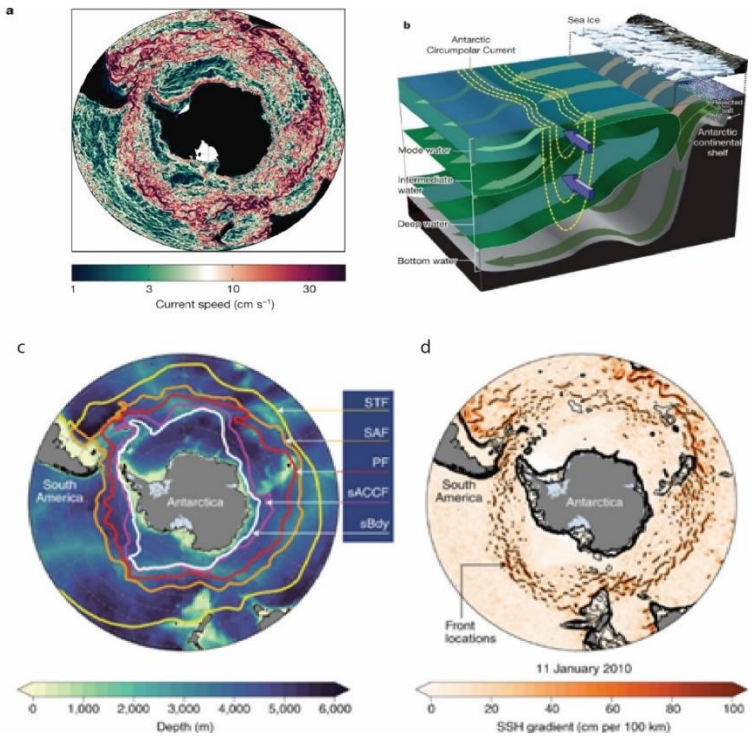

Figure 2. a) Five-day-mean current speed at a depth of 112 m from a high-resolution (1/12°) numerical simulation of the ACC and B) A highly schematic illustration of the Southern Ocean overturning circulation (Rintoul et al., 2018), c) Circumpolar fronts in the southern ocean (Chapman et al., 2020)

Hydrographic data detected three main Southern Ocean fronts, the Subantarctic Front (SAF), the Polar Front (PF), and the Southern ACC Front (sACCF), with the addition of the Subtropical Front (STF) and the Southern Boundary front (SBdy) near Antarctica (Fig. 2c)(Chapman et al., 2020). The STF is the northern boundary of the Southern Ocean and marks the boundary of the northern extent of Subantarctic water as it separates the Subantarctic from Subtropical waters (Fig. 2c). Winds have controlled the position of the front, resulting in seasonal migration of the STF, north to south. The temperatures at the front vary zonally and seasonally by about 4°C, with summer sea surface temperature at approximately 16°C in subtropical waters and 12°C in subantarctic waters, while in the winter is 8°C and 12°C, respectively (Chapman et al., 2020; Sikes et al., 2009a). Different studies (Chadwick, 2022; Sigman et al., 2021; Sikes et al., 2009a) have shown that the Southern Ocean, during the late Pleistocene ice ages, played a role in global cooling, by increasing ocean carbon uptake, thereby lowering atmospheric CO_2 (pCO_2) concentrations, and therefore weakening the global greenhouse effect (Hasenfratz et al., 2019). During the Quaternary, subantarctic waters of the Southern Ocean cooled, and the surface area of the Southern Ocean increased as the fronts migrated northward in the Indian Ocean sector and the Great Australian Bright and Tasmanian regions (Sikes et al., 2009b).

We here provide a detailed reconstruction of the Pliocene-Pleistocene SST evolution of the Subtropical Front based on lipid biomarkers in Ocean Drilling Program (ODP) Site 1168, western Tasmania margin. To assess palaeotemperature records (SST), here we suggest using the TetraEther indeX of tetraethers with 86 atoms (TEX_{86}) and the ketone unsaturation index ($U^{K'}_{37}$) as biomarkers. The TEX_{86} paleothermometer is based on the relative abundance of cyclopentane moieties in isoprenoid glycerol dialkyl glycerol tetraethers (isoprenoid GDGTs) produced by marine archaea (Schouten et al., 2002), while the $U^{K'}_{37}$ index is based on the observation that more di-unsaturated C_{37} alkenone ($C_{37:2}$) than tri-unsaturated C_{37} alkenone ($C_{37:3}$) have been produced by haptophytes algae with increasing growth temperature (Johnson et al., n.d.; Sikes et al., 1991). We propose to use these proxies to identify the trends and the variability of late Pliocene and Pleistocene SSTs at ODP Site 1168 and having this data, we can identify the difference between TEX_{86} and $U^{K'}_{37}$ -based SST reconstructions and the underlying causes of these differences as well as the consequences of the SST changes observed at this site for the oceanographic conditions, specifically the strength and position of the subtropical front. This extra record of SST change will yield a better understanding of the influence of Antarctica and the Southern Ocean on Late Pliocene and Quaternary based on temperature proxies, as the previous studies (Bostock et al., 2015a; Sikes et al., 2009b) followed to the isotope signals which are significantly influenced by other factors, such as seasonality or rainfall.

2. Materials & Methods

2.1 Location & Lithology

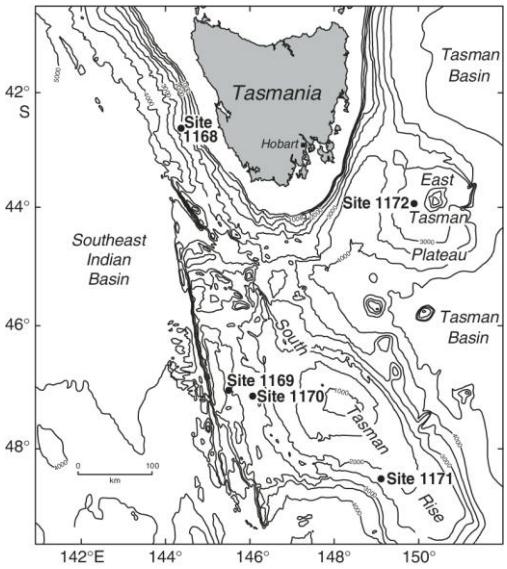

Figure 3. Location map of the site 1168, Source: (Stickley et al., 2004b)

The Ocean Drilling Program (ODP) Site 1168 was one of four drilled during Leg 189 in 2000. It is situated on the 4° slope of Tasmania's western margin (42°38'40"S, 95 144°25'30" E, Fig. 3) in the middle bathyal water depth (2463 m). The sedimentary interval investigated in Hole 1168A has a length of 883.5 mbsf, with a 98 percent average recovery (Exon et al., 2001). Site 1168 was chosen because it represents a continuous sedimentary record (883.5 m) from the early late Eocene to the present. It is located at the intersection of the Tasmante and Sonne seismic reflection lines (Exon et al., 2001). This site was chosen to allow a better understanding of circumpolar oceanographic and climatic evolution.

A nearly continuous 883.5-m-thick interval, drilled at three holes at Site 1168, contains a broad range of sedimentary types that have been classified into five and further into various subunits based on lithological variability. In this study, however, we focus on unit I and subunit IA because their ages range from the late Pliocene to the Pleistocene; Subunit IA was 45 m thick with depths ranging from 0 to 45 mbsf. The sediment of Subunit IA is characterized by light greenish-gray to greenish-gray nannofossil ooze and foraminifera-containing nannofossil ooze. Macrofossil bioclasts and layers of foraminiferal sand were also contained in this subunit. The carbonate content varies from 75 to 95 wt% and bioturbation occurs occasionally and is rarely present in intensity (Exon et al., 2001).

2.2 Samples

For this study, we used 119 samples from Site 1168 on the western edge of Tasmania. These samples were taken from Hole A and taxonomized into Subunit IA (Intervals: Cores 189-1168A-1H to 5H). The depth of those samples ranges between 0 and 32mbsf. The sediments of Subunit IA consist of light greenish-gray to greenish-gray nannofossil ooze and foraminifer-bearing nannofossil ooze. The age of these sediments is late Pliocene to Pleistocene and the main feature is the high content of biogenic carbonates (75-90 wt%) (Exon et al., 2001). Samples were freeze-dried until the extraction. The age model was calculated using R according to Stickley et al. (2004) and it is presented in figure 4 (Stickley et al., 2004a). Magnetostratigraphic data from Hole B, were removed from the age model as there was a discrepancy between them and the $\delta_{18}O$ tie points.

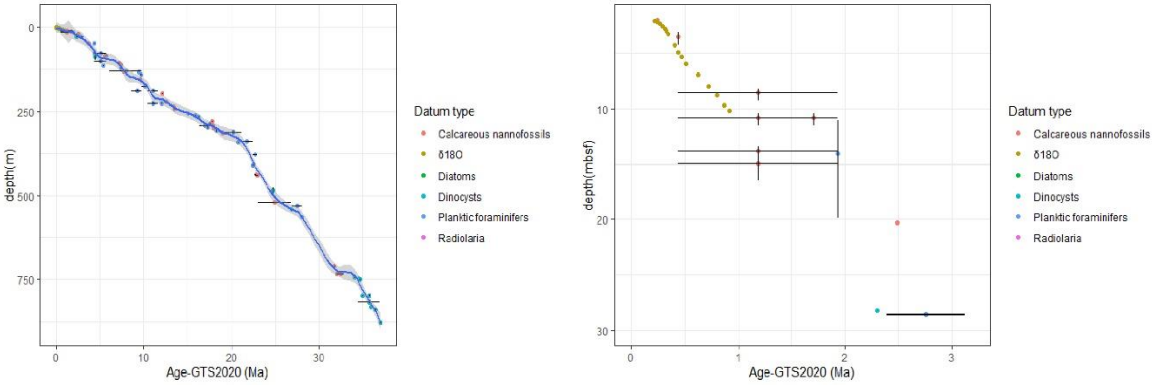

Figure 4. a) Age model of Site 1168 for the last 30 Ma. B) Zoom in age model of Site 1168 for the last 3.2 Ma. Points indicate the datums (Stickley, et al. 2004b). Colours indicate datum types. Blue curve indicates the loess smooth curve with a span of 0.1 throughout the studied interval, which we resampled to obtain ages for the samples used in this study.

2.3 Microwave Extraction

The laboratory analysis aims to determine the presence and the relative abundance of various isoprenoid-branched GDGTs and alkenones in the samples. All sediments were frozen and freeze-dried after sampling; 119 freeze-dried samples were manually powdered to be homogenized and suitable for microwave extraction and were ground prior to weighting. Lipid biomarkers were extracted with Milestone Ethos X microwave system using dichloromethane: methanol (DCM: MeOH) 9:1 (v/v), following the processing of the samples according to Hoem et al. (2021).

Extracts were combined to produce a total lipid extract (TLE), using dichloromethane: methanol (DCM: MeOH) 9:1 (v/v); The TLE was separated onto three different compound classes: apolar/non-polar, neutral/ketones, and polar by using an AlO_x column with the addition of three different solvent mixtures: hexane: DCM 9:1 (v/v), hexane: DCM 1:1 (v/v) and DCM: MeOH 1:1 (v/v), respectively. Therefore, since the compounds can dissolve in these different solvents, they were transported to the AlOx stationary phase, allowing the fractions to be separated from the TLE. When the fractions were ready, the mixtures were subsequently dried under a stream of N_2 to evaporate the solvent and were weighted to determine the amount of fraction collected from each filter.

Polar fractions of the TLE were filtered using a 0.45 um polytetrafluorethylene (PTFE) filter and analyzed using an Agilent 1260 Infinity series HPLC (High-Performance Liquid Chromatography) system coupled to an Agilent 6130 single 372 quadrupole mass spectrometer (MS) as described in Hopmans et al. (2015). Analysis was performed using selective ion monitoring mode (SIM) with known mass-to-charge ratio windows (m/z 1302, 1300, 1298, 1296, 1292, 1050, 1048, 1046, 1036, 1034, 1032, 1022, 1020, 1018, and 744) to target only the protonated molecules used in this analysis. The conditions used for APCI-MS were: nebulizer pressure 60 psig, vaporizer temperature 400 °C, drying gas (N_2) flow 6 L/min and temperature 200 °C, capillary current 4 nA, corona 32 V.

Ketone fractions were analyzed on a Gas Chromatograph (GC) coupled to a flame ionization detector (GC-FID, Hewlett Packard 6890 series) equipped with a CP-Sil 5 fused silica capillary column (25 m x 0.32 mm; film thickness 0.12 um) and a 0.53 mm pre-column. The conditions used for the injection were 70℃, a flow rate of 115 2 ml/min, and helium as a carrier gas. The oven program was as follows: 70℃ for 1 min, then ramped to 130℃ at 20℃ /min, then to 320℃ at 4°C/min, and then held isothermal for 10 mins.

2.4 Data Analysis

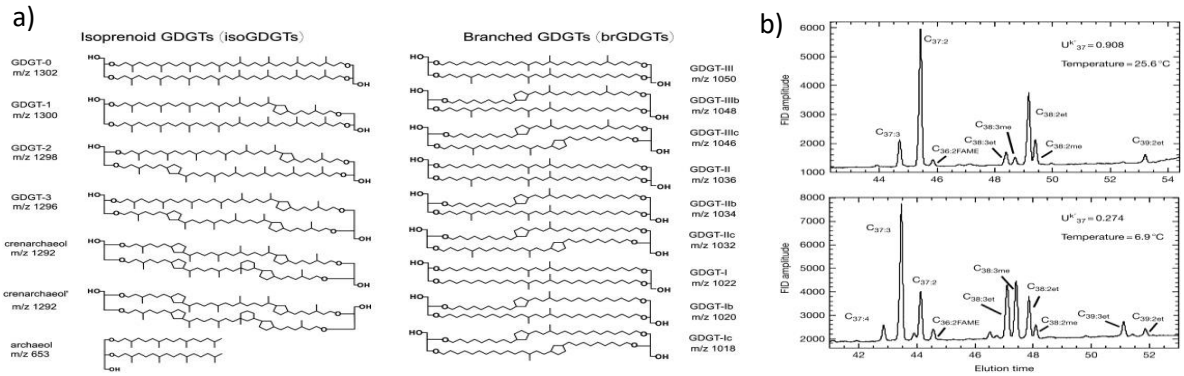

Figure 5. a) Structures of GDGTs and m/z,(Li, et al. 2016) and b) Typical GC–FID chromatograms of alkenone (Herbert, 2014)

Following completion of the required lab analysis, the data set's spectral peaks were integrated to estimate the relative abundances of GDGTs and alkenones; peaks were manually integrated using ChemStation, and indices, as well as ratios for SST reconstructions, were calculated (Bijl et al., 2021). Relative retention times and mass spectra were used to identify isoGDGTs, brGDGTs, H-isoGDGTs, and H-brGDGTs, as well as alkenones (fig. 5).

Table 1. Indices and equations

	Index	Equation	Source
1	TEX_{86}	$\frac{GDGT-2+GDGT-3+Cren'}{GDGT-1+GDGT-2+GDGT-3+Cren'}$	Schouten et al. (2002)
2	$U^{K'}_{37}$	$\frac{[C_{37:2}]}{[C_{37:2}]+[C_{37:3}]}$	Prahl & Wakeham (1987)
3	$BITindex$	$\frac{IIIa+IIIa'+IIa+IIa'+Ia+Ia'}{Cren+IIIa+IIIa'+IIa+IIa'+Ia+Ia'}$	Hopmans et al. (2004)
4	$Methane\ Index$	$\frac{GDGT-1+GDGT-2+GDGT-3}{GDGT-1+GDGT-2+GDGT-3+Cren+Cren'}$	Zhang et al. (2011)
5	$AOM\ ratio$	$\frac{GDGT-2}{Cren}$	Weijers et al. (2011)
6	$Methanogenesis$	$\frac{GDGT-0}{Cren}$	Blaga et al. (2009)
7	$GDGT$-2/3 ratio	$\frac{GDGT-2}{GDGT-3}$	Taylor et al. (2013)
8	$fcren'$	$\frac{\%Cren'}{\%Cren'+\%Cren}$	O'Brien et al. (2017)
9	RI	$0*\%GDGT-0+1*\%GDGT-1+2*\%GDGT-2+3*\%GDGT-3+4*\%Cren+4*\%Cren'$	Zhang et al. (2016)

Initial data were tabulated and organic geochemistry proxies were calculated. To assess palaeotemperature records (SST), TEX86 and UK'37 were used as biomarkers. TEX86 was calculated according to Schouten et al. (2002) (equation 1, Table 1), based on the relative abundance of isoprenoid GDGTs, which included GDGTs with 1,2, and 3 cyclopentane moieties as well as the regio isomer of crenarchaeol. While, UK'37 was determined according to Prahl & Wakeham, (1987b) (Eq. 2, Table 1), by integrating the peak areas of the C37:2 and C37:3 alkenones.

In addition to these proxies, several indices were determined to assess the preservation of GDGTs and their secondary effects. Hopmans et al. (2004) proposed the Branched and Isoprenoid Tetraether (BIT) index, which was used as an indicator of the relative contribution of organic matter in marine sediments, because of the production of isoGDGTs and brGDGTs (Bijl et al., 2021; E. C. Hopmans et al., 2004). The BIT index ranges from 0 (no brGDGTs) to 1 (no Crenarchaeol), based on the relative abundance of terrestrial-derived tetraether lipids versus crenarchaeol (Eq. 3, Table 1). Furthermore, the Methane Index (MI) developed by Zhang et al. (2011) (Eq. 4, Table 1) was used to distinguish between depositional conditions and continental shelves, characterized by anaerobic oxidation of methane (AOM) and diffusive methane flux. Low MI values may indicate that there is no contribution from AOM archaea to the sedimentary GDGT pool, whereas high values (>0.5) indicate hydrate-impacted sediments, and thus corresponding TEX_{86} values should be excluded (O'Brien et al., 2017; Zhang et al., 2011). In addition, the contribution of anaerobic methane oxidizers and methanogenic archaea was identified using the AOM ratio (Eq. 5, Table 1) (Weijers et al., 2011) and Methanogenesis (Eq. 6, Table 1) (Blaga et al., 2009), respectively. GDGT-2/GDGT-3 ratio was used to calculate the contribution of deep-dwelling archaea and the relative cut-off for that is 5, which is the inflection point where TEX_{86} temperature generally agrees with in situ temperature (Hurley et al., 2018). However, modern samples exceed these cutoff values without anomalous TEX86 values based on the Ring Index (Leutert et al., 2021; van der Weijst et al., 2022). According to O'Brien et al. (2017), the fcren' ratio was calculated to explore GDGT distributions in sediments. This proportion is determined by the relative abundance of the crenarchaeol regio-isomer.

Moreover, we applied the Ring Index (RI) (Eq. 9, Table 1), which was proposed by Zhang et al. (2016), to indicate the correlation between ratios. This index is based on the fact that the relative weight of each compound is determined by the number of cyclopentane rings. Lower RI values are associated with GDGT-0 abundance when compared to crenarchaeol, as the GDGT-0/Crenarchaeol ratio is strongly related to RI values (Zhang et al., 2016).

2.5 Calibrations

To convert TEX86 values to sea surface temperatures, several calibrations have been proposed. Here, we apply an exponential calibration proposed by Kim et al. (2010) (Table 2) and the spatial linear Bayesian calibration (Tierney & Tingley, 2014, 2015), using SST (0-20m) and depth-integrated SubT (0-200m) calibrations, because of the spatial distribution characterization. The UK'37 index has been calculated according to Prahl et al. (1987) and converted to SST using the BAYSPLINE calibration (Prahl & Wakeham, 1987b; Tierney & Tingley, 2018). However, after the comparison between those calibrations, BAYSPAR and BAYSPLINE have been used to make the comparison between those biomarkers, as they are more suitable for this site and considered the regional characteristics (Tierney & Tingley, 2014, 2015).

Table 2. Calibration and Equations

Calibration	Equation	Source
SST-$TEX86_{exp}$	$68.4 * log10(TEX_{86}) + 38.6$	Kim et al. (2010)
SST-$U^{K'}_{37}$	$(U^{K'}_{37} - 0.044)/0.033$	Prahl & Wakeham (1987b)
BAYSPAR	TEX_{86} Prior mean: 25, Prior SD: 20	Tierney & Tingley (2015)
BAYSPLINE	$U^{K'}_{37}$ SD: 10	Tierney & Tingley (2018)

3. Results

3.1 GDGTs

The composition of GDGTs is dominated by isoprenoid GDGTs throughout the age model (Fig. 6a) and characterized by the increasing relative abundance of branched GDGTs between 2.8 and 2.5 Ma (Fig. 6b). Isoprenoidal GDGTs are found in high abundance in our dataset compared to br-GDGTs, which is following the normal marine pelagic distribution with crenarchaeol and GDGT-0 the most abundant (Weijers et al., 2011), presenting absolute values between 5,000 and 7,000 ng/g dry sediment, while GDGT-1, 2, and 3 are relatively low with absolute values vary between 0 and 1,000 ng/g dry sediment (Fig. 6c). Crenarchaeol and GDGT-0 present the higher values at approximately 2.2 Ma, 1.9, 1.1 Ma, and 0.2 Ma (Fig. 6c), with a decreasing trend at 2.6 Ma and during the onset of the MPT (~0.9 Ma). However, the most interesting part of this figure (Fig. 6 a, c) is between 1.8 and 1.6 Ma, where crenarchaeol and GDGT-0 seem to be in a stable stage, which maybe reflects the progressive glacial-stage condition.

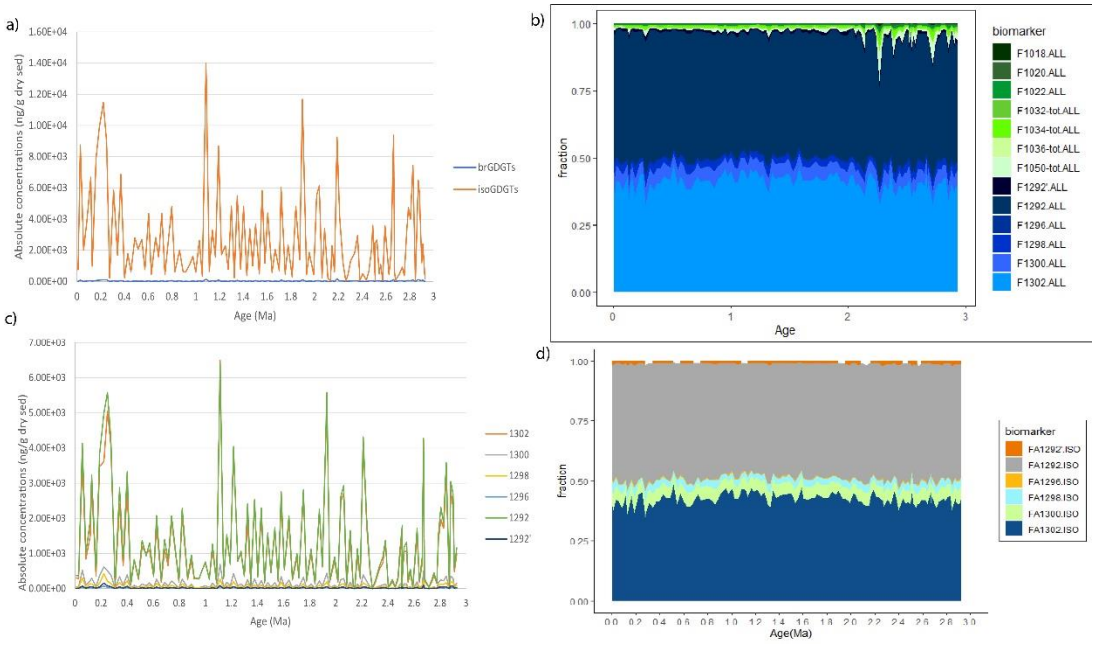

Figure 6. a) Comparison of Iso and br GDGTs absolute concentrations, b) Relative abundance of GDGTs at ODP site 1168, c) Absolute concentrations of isoGDGTs and d) Relative abundance of iso-GDGTs at ODP Site 1168

Before converting TEX_{86} and $U^{K'}_{37}$ into SST, several indices were determined to assess the preservation of GDGTs and their secondary effects. Across the entire record, during Pliocene and Quaternary, the BIT index is relatively low with values varying between 0 and 0.25 (Fig. 7 b) which indicates high Crenarchaeol production in the marine realm and it is associated with in situ marine production of brGDGTs (Sinninghe Damsté, 2016), therefore the brGDGTs are not terrestrial sourced but marine-produced. The former can be also verified by absolute concentrations of GDGTs (Fig. 6) where crenarchaeol is in abundance while the latter is also suggested by the high and elevated #RingsTetra values (Fig. 7 g, Appendix 1), which vary between 0.25 and 0.7. Moreover, there is no overprint from anaerobic methane oxidizers in our samples as none of the samples have methane index (Fig. 7c) values above the thresholds of 0.4 and there also seems to be no derivation from methanogenic archaea (Fig. 7e), as GDGT-0/Crenarchaeol distribution varies between 0 and 1. One of the most significant results in our samples is the GDGT-2/3 ratio. According to Fig. 7 f, only 2 of our samples are below the cut-off of 5; both of them are from the early Pleistocene. The remainder, 118 samples, present extremely high values which are exceeding 5 and vary between 5 and 10.

However, this is not the case for the other indices as all of these samples have values below the threshold values. In addition, the increase in the GDGT-2/3 ratio, from values of c. 5 to a range of c. 6-10, is caused by the increase in the proportions of GDGT-2 (Fig. 7, Appendix 3). Therefore, the GDGDT-2/3 ratio is extremely high which is precisely influenced by the subsurface, and may suggest some contributions of deep-dwelling GDGTs into the mixed layer resulting in some cold bias in TEX_{86} (Fig. 10).

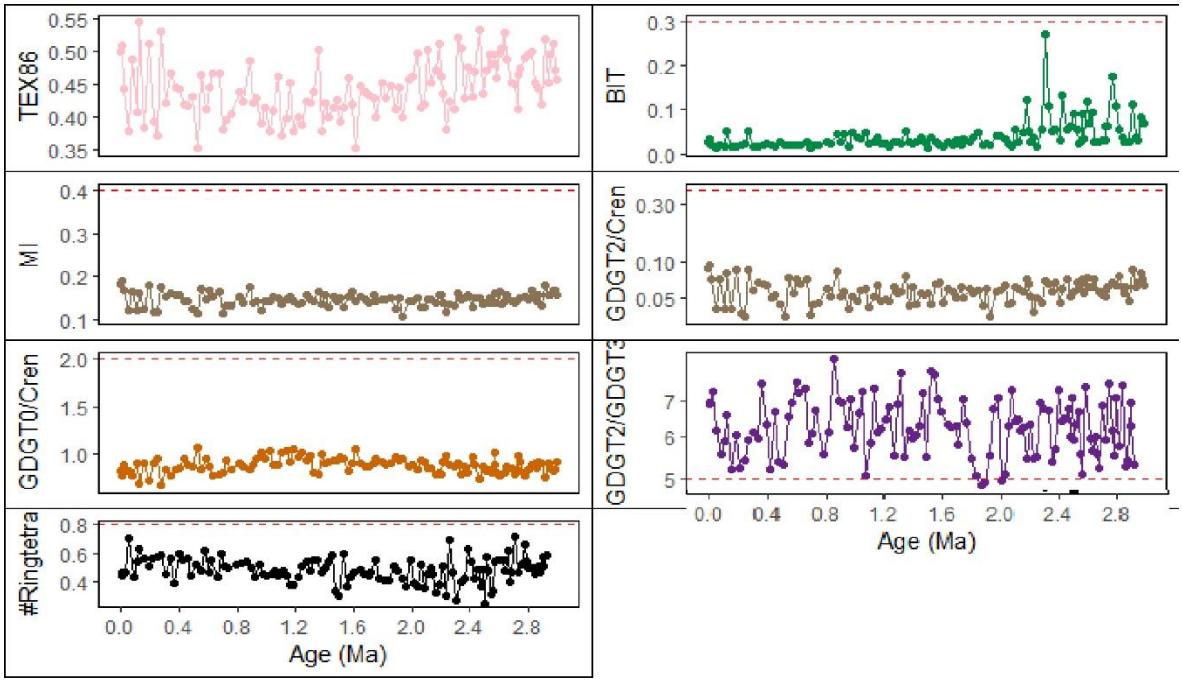

Figure 7. Comparison of different indices at Site 1168. a)TEX86 (Schouten et al., 2002), b) BIT index (Hopmans et al., 2004), c) Methane index (Zhang et al., 2011), D) GDGT2/Cren ratio (Weijers et al., 2011), e) GDGT-0/Cren ratio (Blaga et al., 2009), f) GDGT-2/GDGT-3 ratio (Taylor et al., 2013), g)#Ringtetra. The red lines indicate the cutoff values.

Both TEX_{86} and Ring Index (RI) values generally escalate with increasing SST (Fig. 8), as the distribution of all GDGTs reflects a response to rising temperatures. Moreover, almost all the samples follow the overall $RI=TEX_{86}$ trend, and all of the available TEX_{86} and RI indices are highly correlated when fitted with a quadratic regression (Fig. 8). There is an exception of two samples, which are not following the quadratic regression and both are from the late Quaternary (0.39 and 0.089 Ma), but these are not discarded as the rest of the indices are below the conservative cut-offs and most of the sediments with abnormal RI values are caused by the highly reduced contribution of Cren.

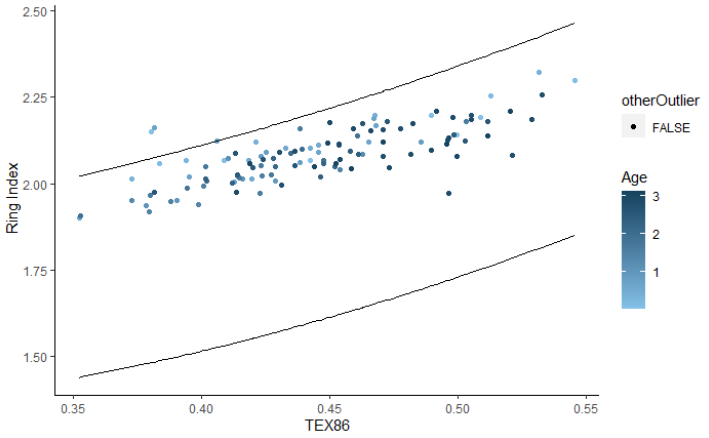

Figure 8. Quadratic regression of TEX_{86} and RI

3.2 Alkenones

The $U^{K'}_{37}$ index records vary between 0.29 to 0.65 and generally follow the trends of TEX_{86}. Late Pliocene sediments have an average $U^{K'}_{37}$ value of ~0.6 with a decreasing trend until the Gauss/ Matuyama boundary (~2.5-2.4 Ma). During the Pleistocene, the $U^{K'}_{37}$ value elevated and declined after the MPT to 0.29. The $U^{K'}_{37}$-based SST shows a warm period, at the end of the Pliocene followed by a cooling trend until 1.3 Ma. After the onset of the MPT (~0.8 Ma), some records show cooler $U^{K'}_{37}$-derived estimates, with SST at approximately 7.5°C (Fig.10). In addition, after 0.2 Ma, there is an increase in the amplitude of the $U^{K'}_{37}$-derived temperature record with an overall warming trend (Fig. 10). Moreover, the two proxy temperature records (TEX_{86} and $U^{K'}_{37}$) are significantly correlated ($R^2=0.84$) and yield similar mean values throughout the records (Fig. 9b), with approximately 13.8°C for $U^{K'}_{37}$ and 14.44°C for TEX_{86} (Fig. 10). There is also a good correlation ($R^2=0.82$) between BAYSPAR and BAYSPLINE calibrations (Fig. 9a), therefore, from now on we use BAYSPAR and BAYSPLINE calibrations for the discussion, as they are more suitable for this Site.

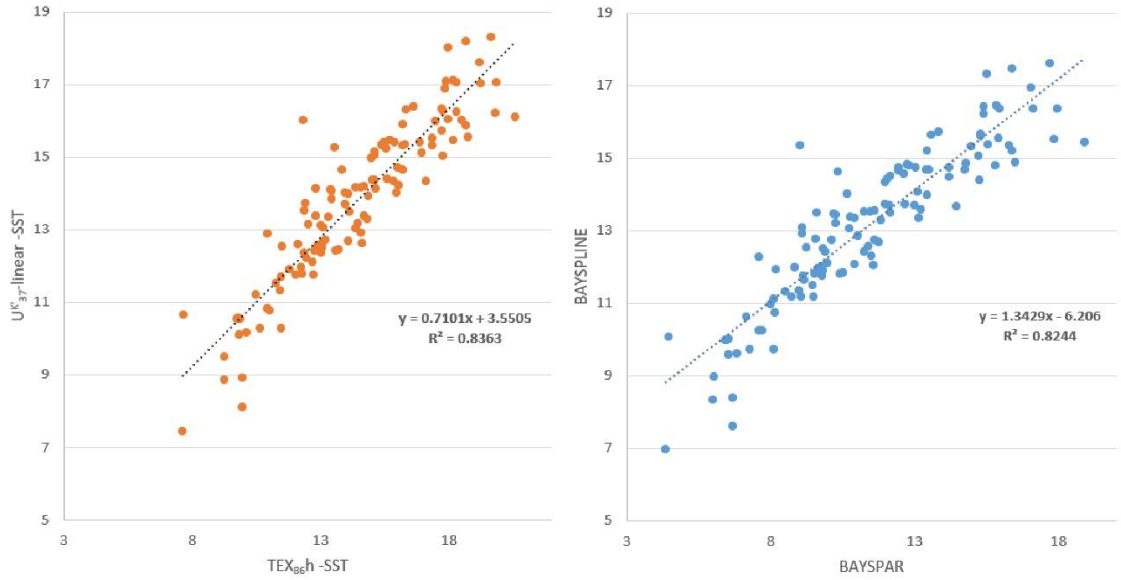

Figure 9. a) Comparison between $U^{K'}_{37}$ linear SST and exponential TEX_{86} calibrations using a linear 1:1 trendline and b) Comparison between BAYSPLINE and BAYSPAR calibration using a linear 1:1 trendline

3.3 SST Reconstructions

Reconstructed SST, using TEX_{86} (Kim et al., 2010) and $U^{K'}_{37}$ (Prahl & Wakeham, 1987b) calibrations, the two proxy temperature records are significantly correlated and yield similar mean values throughout the records. Although our temperature records exhibit an in-phase, glacial-interglacial variability (Fig. 10), display an offset from each other during warm and cold intervals which is as large as ~3-4°C; these offsets are probably due to contributions of deep-dwelling GDGTs into the mixed layer which resulting in some cold bias in TEX_{86} and also calibration uncertainties, but they are consistent to glacial-interglacial variability. At the end of the Pliocene and after 3 Ma, both calibrations present a warming trend with warmer SST TEX_{86}-derived estimates than those from $U^{K'}_{37}$ and an average temperature of approximately 17°C. Following this period and at approximately 2.5 Ma, there is a cooling trend with an average temperature of 12°C, culminating at 2.2 Ma with temperature ranges between 8-12 °C and continuous until 1.3 Ma.

Before the onset of the MPT (~1.3 Ma), both calibrations show a cooling trend with colder SST TEX_{86}-derived estimates than those from $U^{K'}_{37}$, while after the MPT (~0.9 Ma), there is an increase in the amplitude of both calibrations recorded with an overall warming trend until 0.8 Ma, followed by an overall cooling, which culminated at 0.6 Ma until 0.48 Ma and marks the end of the MPT and the last glacial maximum (Fig. 10). Lastly, from 0.47 to 0.3 there is a warming trend with temperatures up to 19 ^{o}C for TEX_{86}-derived estimates and 17^{o}C for $U^{K'}_{37}$.

Overall, SST records decrease from 3 to approximately 1.3 Ma, on average 6 degrees to 4 degrees, and then increase until modern, presenting a constant variability of 3-4 degrees throughout the record. However, the sampling rate varies from 2 to 6 samples per meter of depth which results in a different sampling resolution, specifically, during the early Pleistocene (2.3 Ma) where the amplitude of the difference between these two calibrations (TEX_{86} and $U^{K'}_{37}$) is approximately 4 degrees and during the late Quaternary where the difference is up to 5 degrees. Therefore, we assume that the current sampling resolution is capable of capturing the full amplitude of the variability, except for the early Pleistocene period (2.3 Ma) and further analysis of the intermediate samples will result in a higher resolution.

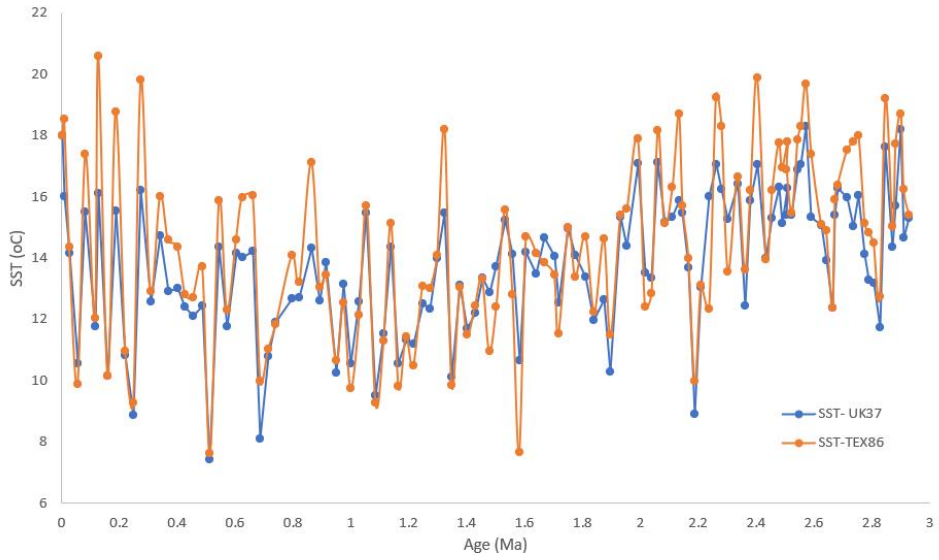

Figure 10. SST-TEX_{86} (Schouten et al. (2002)) and SST- $U^{K'}_{37}$ (Prahl and Wakeham (1987)) Calibrations

4. Discussion

4.1 The reliability of the proxies

In all intervals of the records, all the indices which were determined, present values below the conservative cut-offs. Specifically, as none of the samples have Methane Index (MI) values above thresholds and the GDGT-0/Crenarchaeol distribution is lower than the cut-off of 2 (Fig. 7), we assume that there is no overprint from anaerobic methane oxidizers and there is no derivation from methanogenic archaea, therefore the offsets between TEX_{86} and $U^{K'}_{37}$ could be related to non-thermal factors affecting the TEX_{86} -based SST. The relatively low values of the BIT index, which vary between 0 and 0.25 (Fig. 7b), coupled with the abundance of crenarchaeol reflect low input of soil organic matter to our samples, high Crenarchaeol production in the marine realm and marine-produced br-GDGTs. These can be also verified by absolute concentrations of GDGTs (Fig. 6) and the high and elevated #RingsTetra values (Fig. 7 g, Appendix 1), respectively.

Moreover, the trend and the absolute values of TEX_{86} have not been influenced directly, as throughout the record $U^{K'}_{37}$ -based SST and TEX_{86} -based SST have a great correlation with 3 degrees difference and there is no connection between the difference of two proxy calibrations and the factors contributing to GDGT-2/3 ratio (Figure 11a). Therefore, the suspicion of whether the offset between them is due to increased contributions at lower dwelling GDGTs cannot be proved.

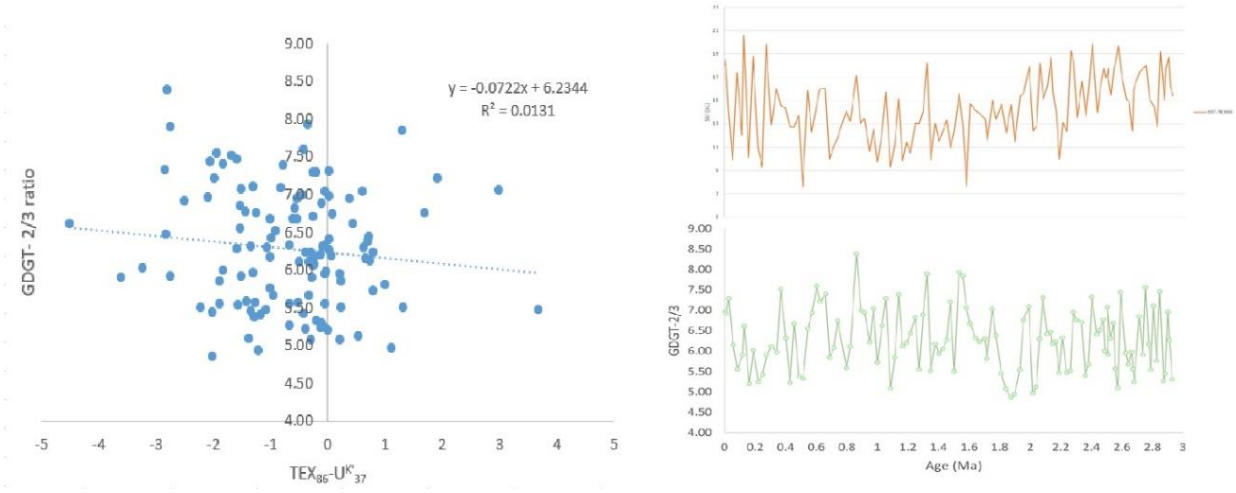

Figure 11. a) GDGT-2/3 ratio distribution versus TEX_{86} and $U^{K'}_{37}$ based SST difference and b) TEX_{86}-based SST and GDGT-2/3 distribution

Although the high GDGT-2/GDGT-3 ratio (values between 5 and 10), except 2 samples which both are from the early Pleistocene (Fig. 7 f), the remainder samples are not discarded as the rest of the ratios are below the threshold values; this increase in the ratio maybe came because of the production of isoGDGTs from other archaea communities, such as haptophyte and Thaumarchaeota (Besseling et al., 2019), increasing proportions of GDGT-2 and resulting to higher values of GDGT-2/GDGT-3 (Appendix 2), which should be associated with lower TEX_{86} values (van der Weijst et al., 2022). Therefore, it is an interesting feature that the cross plot of TEX_{86}-based SST and GDGT-2/3 (Fig. 11 b) presents a positive regression slope, where most of the records show an increase in TEX_{86}-based SST when the GDGT-2/3 ratio is high. Similar relations in the calibration dataset have been found by van der Weijst et al. (2022) and Taylor et al. (2013).

Based on their analysis, they conclude that this is an oceanographical artifact suggesting an influence of non-thermal factors (water column oxygenation and nutrient supply) on GDGT cyclization which is linked to the cold bias in the TEX_{86}-based SST records (Hurley et al., 2018; van der Weijst et al., 2022). Therefore, further analysis of dinocyst assemblages at Site 1168 for this period will be a great suggestion for future studies, as it will verify whether the TEX_{86} variability was driven by non-thermal factors such as upwelling and nutrient supply. Furthermore, both proxies have similar trends and absolute temperatures throughout the records with a constant coherence in the temperature variability which varies between 9 to 18 degrees, therefore, both proxies are dependable. It is an interesting feature in our records, that the TEX_{86} -based SST is in a consistently similar range and usually above the $U^{K'}_{37}$ -based SST throughout most of the records but with the onset of the Pleistocene and during the middle Pleistocene is generally colder than $U^{K'}_{37}$ -based SST. This offset may be associated with non-thermal factors, indicating high variability of upwelling and nutrient supply. Another possible explanation for these offsets could be the calibration uncertainties and the current sampling resolution. As the sampling rates vary from 2 to 6 samples per meter of depth resulting in a different resolution, especially, during the early Pleistocene (2.3 Ma) where the amplitude of the difference between these two calibrations (TEX_{86} and $U^{K'}_{37}$) is approximately 4 degrees and during the late Quaternary where the difference is up to 5 degrees. Therefore, we assume that the current sampling resolution is capable of capturing the full amplitude of the variability, except for the early Pleistocene period (2.3 Ma) and further analysis of the intermediate samples will result in a higher resolution.

4.2 Site 1168 and SST evolution in the Southern Ocean

The SST record of Site 1168 does not follow the trend of the global compilation of the benthic foraminiferal oxygen isotope stack ($\delta^{18}O$) (Westerhold et al., 2020) and the oxygen isotope records on the benthic foraminifers *C. wuellerstorfi and Cibicidoides spp*. on Site 1168 (Nürnberg et al., 2004). Although some temperature records have a good correlation with $\delta^{18}O$ records, however, the latter is much less prominent (Fig. 12). Specifically, the cooling trend from 3 to approximately 1.3 Ma, which is on average 6 degrees to 4 degrees is not visible in the global compilation of the benthic foraminiferal oxygen isotope stack ($\delta^{18}O$) (Westerhold et al., 2020). Moreover, the gradual warming since the MPT (~0.9 Ma till modern) is less prominent on the benthic $\delta^{18}O$ records (Nürnberg et al., 2004). However, the benthic foraminifers *C. wuellerstorfi and Cibicidoides spp*. on Site 1168 which were analyzed by Nürnberg et al., (2004) can help us to recognize some Marine Isotope Stages (MIS), such as MPT (~0.9 Ma), MIS16 (~0.6 Ma), MIS12 (~0.4 Ma) and MIS6 (~0.2 Ma).

Moreover, there is a good correlation between reflectivity (L*) and SST records, SST- BAYSPAR, and SST-BAYSPLINE calibrations, indicating an interesting pattern in our sediment records. During glacial periods, reflectivity depicts lower values while during interglacial periods reflectivity values are higher, therefore, glacial periods characterized by darker sediments records while interglacial are lighter (Fig. 12), as the higher is the reflectance value, the lighter is the color. Although the sediment of Subunit IA of Site 1168 (current samples) is characterized by light greenish gray to greenish gray nannofossil ooze and foraminifera-containing nannofossil ooze, figure 12 may indicate that glacial sediments mainly consist of foraminifera ooze while interglacial sediments mainly contain nannofossil ooze. However, during the Mid and early Pleistocene, there is an offset between these records which is approximately a 1 Ma difference and may be related to the current sampling resolution. The colder intervals of BAYSPAR and BAYSPLINE calibrations are not in accordance with reflectivity records, which may indicate changes in the depositional settings, as there are high reflectance values after the MPT.

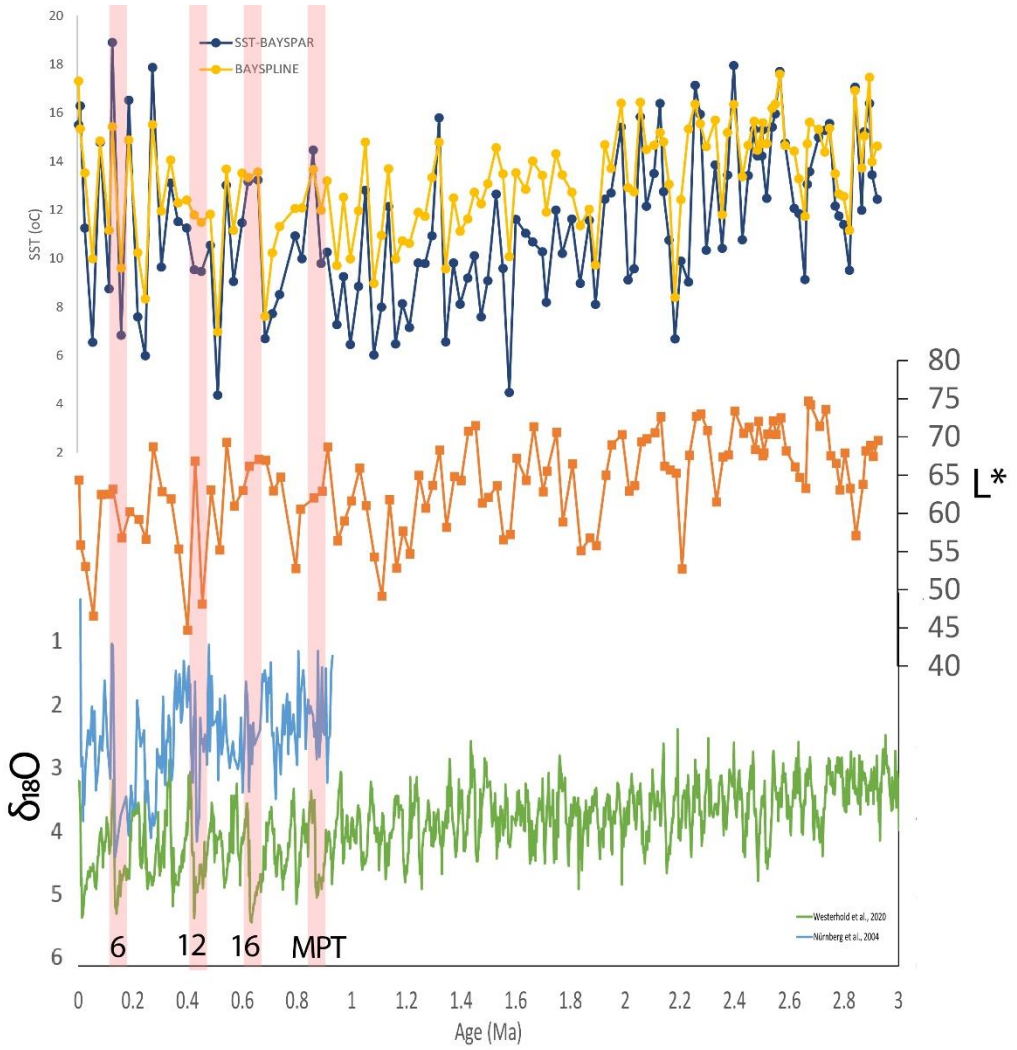

Figure 12. SST reconstructions at site 1168 using BAYSPAR for TEX_{86} and BAYSPLINES for $U^{K'}_{37}$ calibrations in comparison to the global compilation of benthic foraminiferal oxygen isotope stack ($\delta^{18}O$) (Westerhold et al., 2020) and the oxygen isotope records on the benthic foraminifers C. wuellerstorfi and Cibicidoides spp. on Site 1168 (Nürnberg et al., 2004). Glacial periods are highlighted.

Based on the current sampling resolution, after 3 Ma, SSTs of Site 1168 present warm conditions (~17°C-20°C) based on BAYSPAR and BAYSPLINE calibration records which are not following the global $\delta^{18}O$ records as it seems to be stable during this period. Pleistocene records present a progressive cooling up to 3-5°C at 2.8 Ma, with an average temperature of 12°C prior to the onset of Northern Hemisphere glaciation (~2.5 Ma), which was associated with the increase of ice volume between 3.6 and 2.4 Ma, and also the progressive cooling, providing the necessary conditions for major Northern Hemisphere glaciation. The amplitude of this cooling is comparable to other mid-latitude sites, Site 594 (Caballero-Gill et al., 2019) and Site 1125 in the southwest Pacific (Herbert et al., 2016) (Fig. 13), which present higher temperatures compared to Site 1168. This cold period culminated at 2.2 Ma with temperature ranges between 10 and 6 °C, which are less prominent in the global $\delta^{18}O$ records (Westerhold et al., 2020). Following this period and before the onset of the MPT (1.5-1.3 Ma), this cooling trend is continuous but seems more stable compared to the other glacial periods. Thus, the evolution of glacial-interglacial cycles since 1.25 million years ago may have reflected the progress of glacial-stage conditions of the Southern Ocean toward those observed in the glacial maxima of the late Pleistocene (Hasenfratz et al., 2019).

After the MPT (~0.9 Ma) there is an increase in the amplitude of both calibrations, recorded with an overall warming trend and an average temperature of 14°C until 0.7 Ma, where there is a cold period that culminated at 0.6 Ma, presenting extremely cold temperatures for this Site, at approximately ~5-7 °C. This was associated with the transition from the 41kyr obliquity cycle to the 100kyr eccentricity cycle and the reflection of Antarctica's ice sheet during the last glacial maximum, resulting in further cooling of this Site 1168. This cold period lasts until 0.48 Ma and marks the end of the MPT and the last glacial maximum. Furthermore, the temperature difference between subtropical (Site 1125, Site 1168) and subantarctic (Site 594) sites became larger (Fig. 13). Warm conditions appeared again in the late Quaternary (0.4 Ma and 0.2 Ma) with temperature records varying between 18 and 16 °C and with a cold period between 0.3 and 0.1 Ma (Fig. 12). This is in accordance with the SST records for the current period around Tasmania, which are approximately 16°C (Ridgway & Hill, 2009).

In summary, the SST record of the STF is characterized by 5 phases of accelerated, 3-4 degrees cooling, and extremely glacial periods at 2.8 Ma, 2.2 Ma, 1.6 Ma, 0.6 Ma, and 0.4 Ma which are less prominent in the global $\delta^{18}O$ records and the oxygen isotope records on the benthic foraminifers *C. Wuellerstorfi and Cibicidoides spp*. on Site 1168 (Fig. 12). Moreover, it is also a fact that Site 1168 presents a constant variability of 3-4 degrees throughout the records, which is higher than the equatorial sites, as it is located closer to Antarctica, therefore evolutions in Antarctica influences Site 1168.

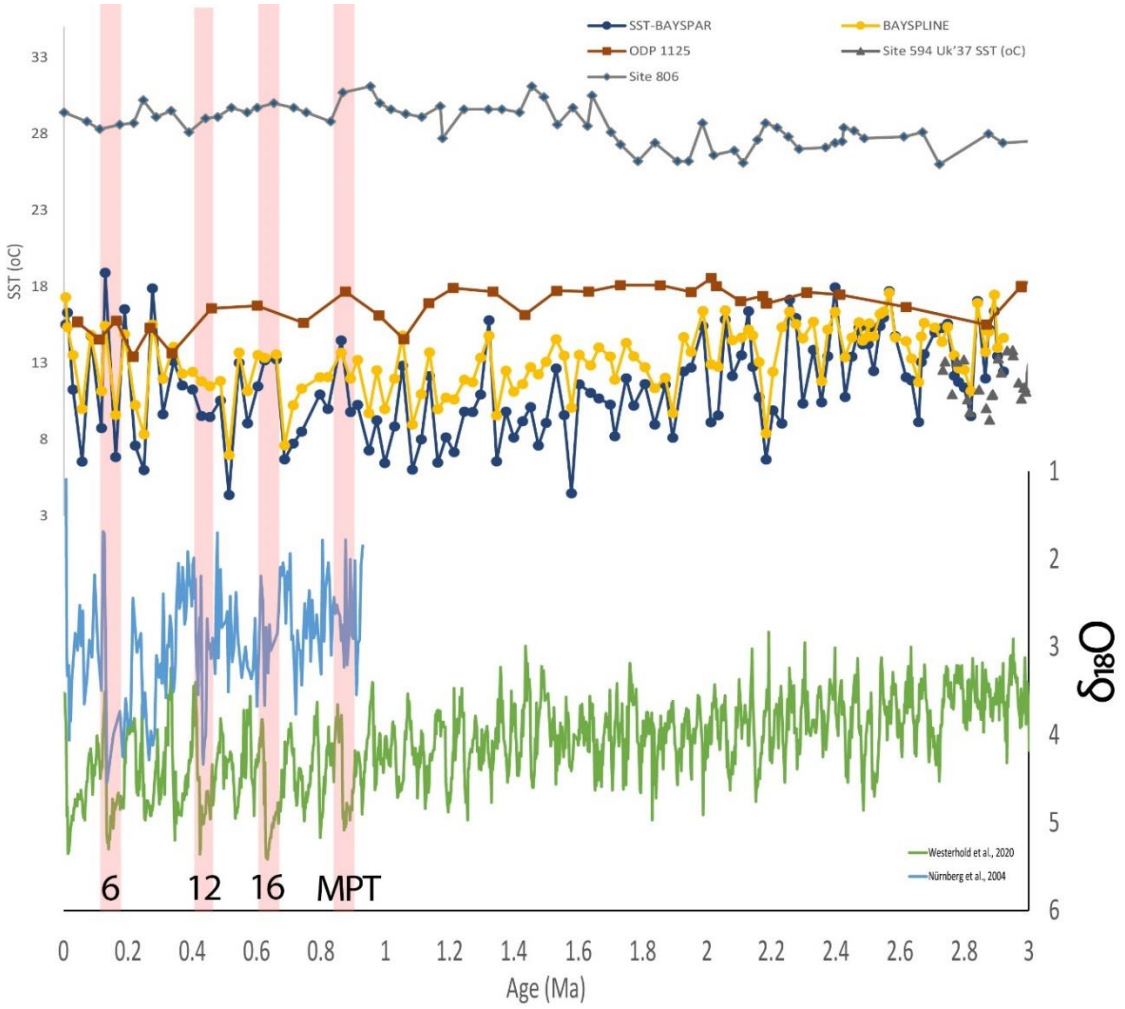

Figure 13. Paleotemperature reconstructions of Site 1168 (this study) using BAYSPAR for TEX_{86} and BAYSPLINES for $U^{K'}_{37}$ calibrations, Site 806 (White and Ravelo 2020), Site 1125 and Site 594 (Caballero-Gill et al., 2019) and the global compilation of benthic foraminiferal oxygen isotope stack ($\delta^{18}O$) (Westerhold et al., 2020) and the oxygen isotope records on the benthic foraminifers C. wuellerstorfi and Cibicidoides spp. on Site 1168 (Nürnberg et al., 2004).

4.3 Subtropical Front

Changes in the sea surface temperatures at Site 1168, located north of the STF in the modern, can indicate the changes in the frontal shifts and the movements and expansion of the Southern Ocean. The different geochemical records which have been used in this study may result in a better understanding and further constrain of oceanographic frontal systems and variations in surface currents in the Pleistocene. Having this data, the most significant changes in palaeoceanography, such as latitudinal migration of STF and variations in surface currents, occurred during glacial periods, especially near the Gauss/ Matuyama boundary (~2.5-2.4 Ma) and during the MPT (0.9 Ma) and the last glacial maximum (0.7-0.5 Ma). As the SST record of the STF is characterized by 5 phases of accelerated, 3-4 degrees cooling, and extremely glacial periods at 2.8 Ma, 2.2 Ma, 1.6 Ma, 0.6 Ma, and 0.4 Ma, here we divide the intervals into 4 stages: 3 to 2.2 Ma, 2.2 to 1.6 Ma, 1.6 to 0.6 Ma and 0.6 to 0 Ma.

- **3 to 2.2 Ma**

In general, late Pliocene SSTs of Site 1168 present warm conditions (~17°C-20°C) based on TEX_{86} and $U^{K'}_{37}$ records, with colder SST $U^{K'}_{37}$-derived estimates than those from TEX_{86}, which are not following the global $\delta^{18}O$ records and roughly correlated to known events, such as mPWP. These overall warmer SSTs may suggest that STF lay to the south of Site 1168, representing a small displacement. However, the early Pleistocene records present a progressive cooling up to 3-5°C at 2.8 Ma, but with colder SST TEX_{86}-derived estimates than those from $U^{K'}_{37}$, which is the case for all glacial periods. The average temperature of this period was approximately 12°C and this glacial lasts until the onset of Northern Hemisphere glaciation (~2.5 Ma). This cold period culminated at 2.2 Ma with temperature ranges between 8 and 6 ^{o}C, which are less prominent in the global $\delta^{18}O$ records. This subsequent cooling (3-5°C) from 2.6 Ma until 2.2 Ma (Fig. 22) coupled with the increase in productivity can reflect a northward displacement of STF.

- **2.2 to 1.6 Ma**

From 2.2 Ma until 1.6 Ma, the cooling trend is continuous but seems more stable compared to the other glacial periods, with some interglacial periods in between. Thus, the evolution of glacial-interglacial cycles since 1.25 million years ago may have reflected the progress of glacial-stage conditions of the Southern Ocean toward those observed in the glacial maxima of the late Pleistocene (Hasenfratz et al., 2019). During this period, the temperature ranges between 16 and 4 ^{o}C and these records suggest a northward displacement of the STF.

- **1.6 to 0.6 Ma**

After 1.6 Ma and since the MPT, the temperature records show a warming trend which is culminating at 1.2Ms and 0.9 Ma with the temperature range between 16 and 6 ^{o}C. The extreme warming observed during the MPT (0.9 Ma) has been linked to a possible collapse of the Antarctic Ice Sheet and a southward shift of the STF. Moreover, this period is characterized by the onset of the dominant 100-kyr eccentricity cycles and coexists with decreases in the offset between the temperature calibrations and progressively higher productivity, during the glacial periods (Cartagena-Sierra et al., 2021). Specifically, the increase in the amplitude of SSTs calibrations after the MPT (0.9 Ma), recorded an overall warming trend and low productivity records, followed by a cooling trend which culminated after the MPT (0.7 Ma). Previous studies from the southwest Pacific Ocean suggest that the STF was located between 3 and 5^{o} further north during the last glacial maximum (Kohfeld et al., 2013) andSikes et al. (2009a) also suggest that the STF located north of the rise (-44^{o}S) close to Tasmania while Bostock

et al. (2015b) suggest that the STF sat north as -37°S. Our trend indicating not only an increase in nutrient supply but also the northward migration of the STF in the Indian Ocean sector and the Great Australian Bright and Tasmanian regions.

- **0.6 to 0 Ma**

This cold period, which started after the MPT, lasts until 0.48 Ma and marks the end of the MPT and the last glacial maximum. Our records indicate that surface water temperatures show glacial-interglacial variability and suggest that latitudinal migrations of the STF still took place during glacial-interglacial periods. Warm conditions appeared again in the late Pleistocene (0.4 Ma and 0.2 Ma) with a cold period between 0.3 and 0.1 Ma (Fig. 22) coupled with the extension of the Antarctic ice sheet and sea ice, resulting in a northward movement of the Subtropical Convergence. During MIS 6, according to Nürnberg et al. (2004), warm SSTs and high productivity records suggested a northward migration and a shift of the Subtropical Convergence to ~44°S. This shift was changed during MIS 2 and the Subtropical Convergence moved north of ~42°S west of Tasmania (Fig. 22).

In summary, the SST record of the STF is characterized by 5 phases of accelerated, 3-4 degrees cooling, and extremely glacial periods at 2.8 Ma, 2.2 Ma, 1.6 Ma, 0.6 Ma, and 0.4 Ma which are less prominent in the global $\delta^{18}O$ records, resulting to the northward migration of the STF and the present location of the Subtropical Convergence.

Conclusion

The SST record from Site 1168, offshore Tasmania, derived from two different biomarker proxies, provides a complete record of Subtropical Southern Ocean SST during the late Pliocene and Quaternary. The SST records reflect a temperate late-Pliocene and a highly variable Pleistocene to the modern, with a gradual ~10°C cooling during the early-mid Pleistocene, stable records during the mid-late Pleistocene, and warming during the late Quaternary. The SST record does not follow the global compilation of the benthic foraminiferal oxygen isotope stack ($\delta^{18}O$) (Westerhold et al., 2020) and the oxygen isotope records on the benthic foraminifers *C. wuellerstorfi and Cibicidoides spp*. on Site 1168 (Nürnberg et al., 2004), with glacial cycles appear less prominent in $\delta^{18}O$ records. In summary, the SST record of the STF is characterized by 5 phases of accelerated, 3-4 degrees cooling, at 2.8 Ma, 2.2 Ma, 1.6 Ma, 0.6 Ma, and 0.4 Ma which are less prominent in the global $\delta^{18}O$ records. According to the shipboard, reflectivity values our sediments of glacial periods mainly consist of foraminifera ooze while interglacial sediments mainly contain nannofossil ooze.

Comparing SST records and using records from previous studies we have a better understanding of oceanographic frontal systems and surface currents in Tasmania. The most significant changes occurred during glacial periods with the incursion of nutrient-rich Subantarctic Surface Water to Subtropical Convergence, resulting in northward movement of STF and a shift of the Subtropical Convergence to ~42°S west of Tasmania.

References

Besseling, E., Redondo-Hasselerharm, P., Foekema, E. M., & Koelmans, A. A. (2019). Quantifying ecological risks of aquatic micro-and nanoplastic. *Critical Reviews in Environmental Science and Technology*, *49*(1), 32–80.

Bijl, P. K., Frieling, J., Cramwinckel, M. J., Boschman, C., Sluijs, A., & Peterse, F. (2021). Maastrichtian–Rupelian paleoclimates in the southwest Pacific – a critical re-evaluation of biomarker paleothermometry and dinoflagellate cyst paleoecology at Ocean Drilling Program Site 1172. *Clim. Past*, *17*(6), 2393–2425. https://doi.org/10.5194/cp-17-2393-2021

Blaga, C. I., Reichart, G.-J., Heiri, O., & Sinninghe Damsté, J. S. (2009). Tetraether membrane lipid distributions in water-column particulate matter and sediments: a study of 47 European lakes along a north–south transect. *Journal of Paleolimnology*, *41*(3), 523–540. https://doi.org/10.1007/s10933-008-9242-2

Bostock, H. C., Hayward, B. W., Neil, H. L., Sabaa, A. T., & Scott, G. H. (2015a). Changes in the position of the Subtropical Front south of New Zealand since the last glacial period. *Paleoceanography*, *30*(7), 824–844. https://doi.org/https://doi.org/10.1002/2014PA002652

Bostock, H. C., Hayward, B. W., Neil, H. L., Sabaa, A. T., & Scott, G. H. (2015b). Changes in the position of the Subtropical Front south of New Zealand since the last glacial period. *Paleoceanography*, *30*(7), 824–844. https://doi.org/https://doi.org/10.1002/2014PA002652

Caballero-Gill, R. P., Herbert, T. D., & Dowsett, H. J. (2019). 100-kyr Paced Climate Change in the Pliocene Warm Period, Southwest Pacific. *Paleoceanography and Paleoclimatology*, *34*(4), 524–545. https://doi.org/https://doi.org/10.1029/2018PA003496

Cartagena-Sierra, A., Berke, M. A., Robinson, R. S., Marcks, B., Castañeda, I. S., Starr, A., Hall, I. R., Hemming, S. R., LeVay, L. J., & Party, E. 361 S. (2021). Latitudinal Migrations of the Subtropical Front at the Agulhas Plateau Through the Mid-Pleistocene Transition. *Paleoceanography and Paleoclimatology*, *36*(7), e2020PA004084.

Chadwick, M. (2022). Reconstructing Antarctic sea ice from 130,000 years ago. *Past Global Changes Magazine*, *30*(2), 86–87.

Chapman, C. C., Lea, M.-A., Meyer, A., Sallée, J.-B., & Hindell, M. (2020). Defining Southern Ocean fronts and their influence on biological and physical processes in a changing climate. *Nature Climate Change*, *10*(3), 209–219.

Da, J., Zhang, Y. G., Li, G., Meng, X., & Ji, J. (2019). Low CO2 levels of the entire Pleistocene epoch. *Nature Communications*, *10*(1), 4342. https://doi.org/10.1038/s41467-019-12357-5

Exon, N. F., Kennett, J. P., Malone, M. J., Brinkhuis, H., Chaproniere, G. C. H., Ennyu, A., & Shevenell, A. E. (2001). *The Tasmanian Gateway: Cenozoic climatic and oceanographic development*.

Ford, H. L., & Chalk, T. B. (2020). The Mid-Pleistocene Enigma. *Oceanography*, *33*(2), 101–103.

Ford, H. L., Sosdian, S. M., Rosenthal, Y., & Raymo, M. E. (2016). Gradual and abrupt changes during the Mid-Pleistocene Transition. *Quaternary Science Reviews*, *148*, 222–233.

Hasenfratz, A. P., Jaccard, S. L., Martínez-García, A., Sigman, D. M., Hodell, D. A., Vance, D., Bernasconi, S. M., Kleiven, H. (Kikki) F., Haumann, F. A., & Haug, G. H. (2019). The residence time of Southern Ocean surface waters and the 100,000-year ice age cycle. *Science*, *363*(6431), 1080–1084.

Head, M. J., Gibbard, P., & Salvador, A. (2008). The Quaternary: its character and definition. *International Union of Geological Sciences*, *31*(2), 234–238. https://doi.org/10.18814/epiiugs/2008/v31i2/009

Herbert, T. D. (2014). 8.15 - Alkenone Paleotemperature Determinations. In H. D. Holland & K. K. Turekian (Eds.), *Treatise on Geochemistry (Second Edition)* (pp. 399–433). Elsevier. https://doi.org/https://doi.org/10.1016/B978-0-08-095975-7.00615-X

Herbert, T. D., Lawrence, K. T., Tzanova, A., Peterson, L. C., Caballero-Gill, R., & Kelly, C. S. (2016). Late Miocene global cooling and the rise of modern ecosystems. *Nature Geoscience*, *9*(11), 843–847. https://doi.org/10.1038/ngeo2813

Hodell, D. A., & Venz-Curtis, K. A. (2006). Late Neogene history of deepwater ventilation in the Southern Ocean. *Geochemistry, Geophysics, Geosystems*, *7*(9). https://doi.org/https://doi.org/10.1029/2005GC001211

Hodell, D. A., & Warnke, D. A. (1991). Climatic evolution of the Southern Ocean during the Pliocene epoch from 4.8 to 2.6 million years ago. *Quaternary Science Reviews*, *10*(2), 205–214. https://doi.org/https://doi.org/10.1016/0277-3791(91)90019-Q

Hoem, F. S., Sauermilch, I., Hou, S., Brinkhuis, H., Sangiorgi, F., & Bijl, P. K. (2021). Late Eocene–early Miocene evolution of the southern Australian subtropical front: a marine palynological approach. *Journal of Micropalaeontology*, *40*(2), 175–193.

Hopmans, E. C., Weijers, J. W. H., Schefuß, E., Herfort, L., Sinninghe Damsté, J. S., & Schouten, S. (2004). A novel proxy for terrestrial organic matter in sediments based on branched and isoprenoid tetraether lipids. *Earth and Planetary Science Letters*, *224*(1), 107–116. https://doi.org/https://doi.org/10.1016/j.epsl.2004.05.012

Hopmans, E., Schouten, S., & Sinninghe-Damste, J. (2015). The effect of improved chromatography on GDGT-based palaeoproxies. *Organic Geochemistry*, *93*. https://doi.org/10.1016/j.orggeochem.2015.12.006

Hurley, S. J., Lipp, J. S., Close, H. G., Hinrichs, K.-U., & Pearson, A. (2018). Distribution and export of isoprenoid tetraether lipids in suspended particulate matter from the water column of the Western Atlantic Ocean. *Organic Geochemistry*, *116*, 90–102. https://doi.org/https://doi.org/10.1016/j.orggeochem.2017.11.010

Johnson, A., Williams, M., & Riesselman, C. R. (n.d.). *The PRISM (Pliocene palaeoclimate)*.

Kim, J.-H., van der Meer, J., Schouten, S., Helmke, P., Willmott, V., Sangiorgi, F., Koç, N., Hopmans, E. C., & Damsté, J. S. S. (2010). New indices and calibrations derived from the distribution of crenarchaeal isoprenoid tetraether lipids: Implications for past sea surface temperature reconstructions. *Geochimica et Cosmochimica Acta*, *74*(16), 4639–4654. https://doi.org/https://doi.org/10.1016/j.gca.2010.05.027

Kohfeld, K. E., Graham, R. M., de Boer, A. M., Sime, L. C., Wolff, E. W., le Quéré, C., & Bopp, L. (2013). Southern Hemisphere westerly wind changes during the Last Glacial Maximum: paleo-data synthesis. *Quaternary Science Reviews*, *68*, 76–95.

Leutert, T. J., Modestou, S., Bernasconi, S. M., & Meckler, A. N. (2021). Southern Ocean bottom-water cooling and ice sheet expansion during the middle Miocene climate transition. *Climate of the Past*, *17*(5), 2255–2271. https://doi.org/10.5194/cp-17-2255-2021

Lisiecki, L. E., & Raymo, M. E. (2007). Plio–Pleistocene climate evolution: trends and transitions in glacial cycle dynamics. *Quaternary Science Reviews*, *26*(1), 56–69. https://doi.org/https://doi.org/10.1016/j.quascirev.2006.09.005

Nürnberg, D., Brughmans, N., Schönfeld, J., Ninnemann, U., & Dullo, C. (2004). Paleo-export production, terrigenous flux and sea surface temperatures around Tasmania-implications for Glacial/Interglacial changes in the Subtropical Convergence Zone. *The Cenozoic Southern Ocean: Tectonics, Sedimentation, and Climate Change Between Australia and Antarctica, Geophys. Monogr. Ser*, *151*, 291–317.

O'Brien, C. L., Robinson, S. A., Pancost, R. D., Sinninghe Damsté, J. S., Schouten, S., Lunt, D. J., Alsenz, H., Bornemann, A., Bottini, C., Brassell, S. C., Farnsworth, A., Forster, A., Huber, B. T., Inglis, G. N., Jenkyns, H. C., Linnert, C., Littler, K., Markwick, P., McAnena, A., … Wrobel, N. E. (2017). Cretaceous sea-surface temperature evolution: Constraints from TEX86 and planktonic foraminiferal oxygen isotopes. *Earth-Science Reviews*, *172*, 224–247. https://doi.org/https://doi.org/10.1016/j.earscirev.2017.07.012

Prahl, F. G., & Wakeham, S. G. (1987a). Calibration of unsaturation patterns in long-chain ketone compositions for palaeotemperature assessment. *Nature*, *330*(6146), 367–369. https://doi.org/10.1038/330367a0

Prahl, F. G., & Wakeham, S. G. (1987b). Calibration of unsaturation patterns in long-chain ketone compositions for palaeotemperature assessment. *Nature*, *330*(6146), 367–369. https://doi.org/10.1038/330367a0

Ridgway, K., & Hill, K. (2009). *The East Australian Current*.

Rintoul, S. R. (2018). The global influence of localized dynamics in the Southern Ocean. *Nature*, *558*(7709), 209–218.

Sallée, J.-B. (2018). Southern ocean warming. *Oceanography*, *31*(2), 52–62.

Schouten, S., Hopmans, E. C., Schefuß, E., & Damste, J. S. S. (2002). Distributional variations in marine crenarchaeotal membrane lipids: a new tool for reconstructing ancient sea water temperatures? *Earth and Planetary Science Letters*, *204*(1–2), 265–274.

Sigman, D. M., Fripiat, F., Studer, A. S., Kemeny, P. C., Martínez-García, A., Hain, M. P., Ai, X., Wang, X., Ren, H., & Haug, G. H. (2021). The Southern Ocean during the ice ages: A review of the Antarctic surface isolation hypothesis, with comparison to the North Pacific. *Quaternary Science Reviews*, *254*, 106732.

Sikes, E. L., Farrington, J. W. t, & Keigwin, L. D. (1991). Use of the alkenone unsaturation ratio U37K to determine past sea surface temperatures: core-top SST calibrations and methodology considerations. *Earth and Planetary Science Letters*, *104*(1), 36–47.

Sikes, E. L., Howard, W. R., Samson, C. R., Mahan, T. S., Robertson, L. G., & Volkman, J. K. (2009a). Southern Ocean seasonal temperature and Subtropical Front movement on the South Tasman Rise in the late Quaternary. *Paleoceanography*, *24*(2).

Sikes, E. L., Howard, W. R., Samson, C. R., Mahan, T. S., Robertson, L. G., & Volkman, J. K. (2009b). Southern Ocean seasonal temperature and Subtropical Front movement on the South Tasman Rise in the late Quaternary. *Paleoceanography*, *24*(2).

Sinninghe Damsté, J. S. (2016). Spatial heterogeneity of sources of branched tetraethers in shelf systems: The geochemistry of tetraethers in the Berau River delta (Kalimantan, Indonesia). *Geochimica et Cosmochimica Acta*, *186*, 13–31. https://doi.org/https://doi.org/10.1016/j.gca.2016.04.033

Stickley, C. E., Brinkhuis, H., McGonigal, K. L., Chaproniere, G. C. H., Fuller, M., Kelly, D. C., Nürnberg, D., Pfuhl, H. A., Schellenberg, S. A., & Schönfeld, J. (2004). Late Cretaceous–Quaternary biomagnetostratigraphy of ODP Sites 1168, 1170, 1171, and 1172, Tasmanian Gateway. *Proceedings of the Ocean Drilling Program, Scientific Results*, *189*, 1–57.

Stickley, C. E., Brinkhuis, H., Schellenberg, S. A., Sluijs, A., Röhl, U., Fuller, M., Grauert, M., Huber, M., Warnaar, J., & Williams, G. L. (2004). Timing and nature of the deepening of the Tasmanian Gateway. *Paleoceanography*, *19*(4).

Taylor, K. W. R., Huber, M., Hollis, C. J., Hernandez-Sanchez, M. T., & Pancost, R. D. (2013). Re-evaluating modern and Palaeogene GDGT distributions: Implications for SST reconstructions. *Global and Planetary Change*, *108*, 158–174. https://doi.org/https://doi.org/10.1016/j.gloplacha.2013.06.011

Tierney, J. E., & Tingley, M. P. (2014). A Bayesian, spatially-varying calibration model for the TEX86 proxy. *Geochimica et Cosmochimica Acta*, *127*, 83–106. https://doi.org/https://doi.org/10.1016/j.gca.2013.11.026

Tierney, J. E., & Tingley, M. P. (2015). A TEX86 surface sediment database and extended Bayesian calibration. *Scientific Data*, *2*(1), 150029. https://doi.org/10.1038/sdata.2015.29

Tierney, J. E., & Tingley, M. P. (2018). BAYSPLINE: A New Calibration for the Alkenone Paleothermometer. *Paleoceanography and Paleoclimatology*, *33*(3), 281–301. https://doi.org/https://doi.org/10.1002/2017PA003201

van der Weijst, C. M. H., van der Laan, K. J., Peterse, F., Reichart, G.-J., Sangiorgi, F., Schouten, S., Veenstra, T. J. T., & Sluijs, A. (2022). A 15-million-year surface- and subsurface-integrated TEX_86 temperature record from the eastern equatorial Atlantic. *Climate of the Past*, *18*(8), 1947–1962. https://doi.org/10.5194/cp-18-1947-2022

Weijers, J. W. H., Lim, K. L. H., Aquilina, A., Sinninghe Damsté, J. S., & Pancost, R. D. (2011). Biogeochemical controls on glycerol dialkyl glycerol tetraether lipid distributions in sediments characterized by diffusive methane flux. *Geochemistry, Geophysics, Geosystems*, *12*(10). https://doi.org/https://doi.org/10.1029/2011GC003724

Westerhold, T., Marwan, N., Drury, A. J., Liebrand, D., Agnini, C., Anagnostou, E., Barnet, J. S. K., Bohaty, S. M., de Vleeschouwer, D., Florindo, F., Frederichs, T., Hodell, D. A., Holbourn, A. E., Kroon, D., Lauretano, V., Littler, K., Lourens, L. J., Lyle, M., Pälike, H., … Zachos, J. C. (2020). An astronomically dated record of Earth's climate and its predictability over the last 66 million years. *Science*, *369*(6509), 1383–1387. https://doi.org/10.1126/science.aba6853

Zhang, Y. G., Pagani, M., & Wang, Z. (2016). Ring Index: A new strategy to evaluate the integrity of TEX86 paleothermometry. *Paleoceanography*, *31*(2), 220–232. https://doi.org/https://doi.org/10.1002/2015PA002848

Zhang, Y. G., Zhang, C. L., Liu, X.-L., Li, L., Hinrichs, K.-U., & Noakes, J. E. (2011). Methane Index: A tetraether archaeal lipid biomarker indicator for detecting the instability of marine gas hydrates. *Earth and Planetary Science Letters*, *307*(3), 525–534. https://doi.org/https://doi.org/10.1016/j.epsl.2011.05.031

Appendix

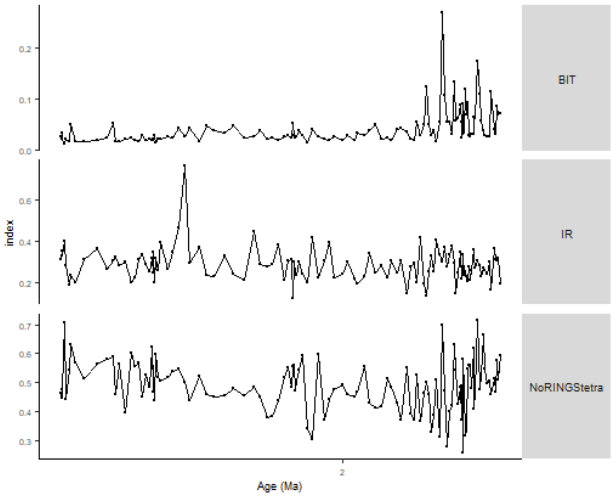

Appendix 1. Comparison of different ratios: a) BIT index, b) IR, c) Ringstetra

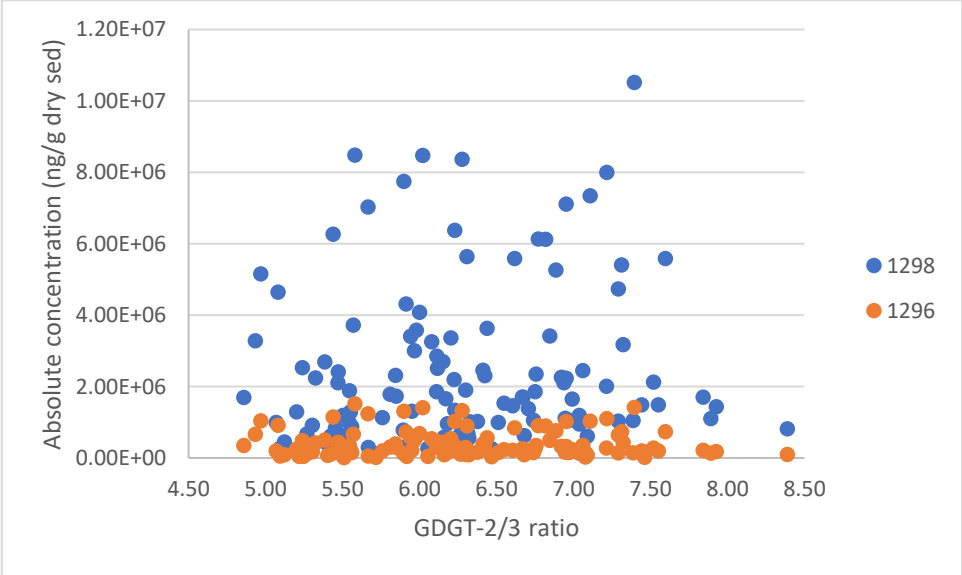

Appendix 2 Absolute concentrations of GDGT-2 and GDGT-3